

The electromagnetics of light transmission through subwavelength slits in metallic films

John Weiner*

Center for Nanoscale Science and Technology, National Institute of Standards and Technology, 100 Bureau Drive, Stop 6203, Gaithersburg, MD 20899, USA
and IFSC-INO, Universidade de São Paulo, CP 369, São Carlos-SP, CEP 13560-970, Brazil

[*johweiner@gmail.com](mailto:johweiner@gmail.com)

Abstract

By numerically calculating the relevant electromagnetic fields and charge current densities, we show how local charges and currents near subwavelength structures govern light transmission through subwavelength apertures in a real metal film. The illumination of a single aperture generates surface waves; and in the case of slits, generates them with high efficiency and with a phase close to $-\pi$ with respect to a reference standing wave established at the metal film front facet. This phase shift is due to the direction of induced charge currents running within the slit walls. The surface waves on the entrance facet interfere with the standing wave. This interference controls the profile of the transmission through slit pairs as a function of their separation. We compare the calculated transmission profile for a two-slit array to simple interference models and measurements [?].

OCIS codes: Optics at surfaces (240.0240); Surface plasmons (240.6680); Surface waves (240.6690)

References and links

1. D. Pacifici, H. J. Lezec, H. A. Atwater, and J. Weiner, "Quantitative determination of optical transmission through subwavelength slit arrays in Ag films: Role of surface wave interference and local coupling between adjacent slits," *Phys. Rev. B* **77**(11), 115411 (2008).
2. J. Weiner, "The physics of light transmission through subwavelength apertures and aperture arrays," *Rep. Prog. Phys.* **72**(6), 064401 (2009).
3. M. W. Kim, T. T. Kim, J. E. Kim, and H. Y. Park, "Surface plasmon polariton resonance and transmission enhancement of light through subwavelength slit arrays in metallic films," *Opt. Express* **17**(15), 12315–12322 (2009).
4. I. S. Spevak, A. Y. Nikitin, E. V. Bezuglyi, A. Levchenko, and A. V. Kats, "Resonantly suppressed transmission and anomalously enhanced light absorption in periodically modulated ultrathin metal films," *Phys. Rev. B* **79**(16), 161406 (2009).
5. S. Collin, C. Sauvan, C. Billaudeau, F. Pardo, J. C. Rodier, J. L. Pelouard, and P. Lalanne, "Surface modes on nanostructured metallic surfaces," *Phys. Rev. B* **79**(16), 165405 (2009).
6. J. S. White, G. Veronis, Z. F. Yu, E. S. Barnard, A. Chandran, S. H. Fan, and M. L. Brongersma, "Extraordinary optical absorption through subwavelength slits," *Opt. Lett.* **34**(5), 686–688 (2009).
7. P. B. Catrysse and S. H. Fan, "Propagating plasmonic mode in nanoscale apertures and its implications for extraordinary transmission," *J. Nanophotonics* **2**, 021790 (2008).
8. R. Marques, F. Mesa, L. Jelinek, and F. Medina, "Analytical theory of extraordinary transmission through metallic diffraction screens perforated by small holes," *Opt. Express* **17**(7), 5571–5579 (2009).
9. J. Fiala and I. Richter, "Interaction of light with subwavelength apertures: a comparison of approximate and rigorous approaches," *Opt. Quant. Electron.* **41**(5), 409–427 (2009).
10. V. E. Babicheva and Y. E. Lozovik, "Role of propagating slit mode in enhanced transmission through slit arrays in a metallic films," *Opt. Quant. Electron.* **41**(4), 299–313 (2009).
11. X. F. Li and S. F. Yu, "Long-wavelength optical transmission of extremely narrow slits via hybrid surface-plasmon and Fabry-Perot modes," *J. Appl. Phys.* **108**(1), 013302 (2010).

12. R. L. Chern and W. T. Hong, "Transmission resonances and antiresonances in metallic arrays of compound subwavelength holes," *J. Optics* **12**(6), 065101 (2010).
13. Z. Y. Wei, J. X. Fu, Y. Cao, C. Wu, and H. Q. Li, "The impact of local resonance on the enhanced transmission and dispersion of surface resonances," *Photonic. Nanostruct.* **8**(2), 94–101 (2010).
14. M. Diwekar, S. Blair, and M. Davis, "Increased light gathering capacity of sub-wavelength conical metallic apertures," *J. Nanophotonics* **4**, 043504 (2010).
15. B. Wang and P. Lalanne, "Surface plasmon polaritons locally excited on the ridges of metallic gratings," *J. Opt. Soc. Am. A* **27**(6), 1432–1441 (2010).
16. P. Banzer, J. Kindler, S. Quabis, U. Peschel, and G. Leuchs, "Extraordinary transmission through a single coaxial aperture in a thin metal film," *Opt. Express* **18**(10), 10,896–10,904 (2010).
17. Y. L. Hua, J. X. Fu, J. Y. Li, Z. Y. Li, and H. F. Yang, "Experimental studies of extraordinary light transmission through periodic arrays of subwavelength square and rectangular holes in metal films," *Chinese Phys. B* **19**(4), 047,309 (2010).
18. Y. S. Zhou, B. Y. Gu, H. Y. Wang, and L. M. Zhao, "Enhancement of the extraordinary optical transmission in a subwavelength metal slit dressed by a metal grating," *Phys. Rev. A* **81**(3), 035,803 (2010).
19. V. Delgado, R. Marques, and L. Jelinek, "Analytical theory of extraordinary optical transmission through realistic metallic screens," *Opt. Express* **18**(7), 6506–6515 (2010).
20. R. Gordon, A. G. Brolo, D. Sinton, and K. L. Kavanagh, "Resonant optical transmission through hole-arrays in metal films: physics and applications," *Laser Photonics Rev.* **4**(2), 311–335 (2010).
21. M. A. Vincenti, D. de Ceglia, M. Buncick, N. Akozbek, M. J. Bloemer, and M. Scalora, "Extraordinary transmission in the ultraviolet range from subwavelength slits on semiconductors," *J. Appl. Phys.* **107**(5), 053,101 (2010).
22. X. R. Huang and R. W. Peng, "General mechanism involved in subwavelength optics of conducting microstructures: charge-oscillation-induced light emission and interference," *J. Opt. Soc. Am. A* **27**(4), 718–729 (2010).
23. M. J. Kofke, D. H. Waldeck, Z. Fakhraai, S. Ip, and G. C. Walker, "The effect of periodicity on the extraordinary optical transmission of annular aperture arrays," *Appl. Phys. Lett.* **94**(2), 023104 (2009).
24. P. B. Catrysse and S. H. Fan, "Understanding the dispersion of coaxial plasmonic structures through a connection with the planar metal-insulator-metal geometry," *Appl. Phys. Lett.* **94**(23), 231111 (2009).
25. F. I. Baida, Y. Poujet, J. Salvi, D. Van Labeke, and B. Guizal, "Extraordinary transmission beyond the cut-off through sub-lambda annular aperture arrays," *Opt. Comm.* **282**(7), 1463–1466 (2009).
26. E. Feigenbaum and H. A. Atwater, "Resonant Guided Wave Networks," *Phys. Rev. Lett.* **104**(14), 147,402 (2010).
27. F. J. Garcia-Vidal, L. Martin-Moreno, T. W. Ebbesen, and L. Kuipers, "Light passing through subwavelength apertures," *Rev. Mod. Phys.* **82**(1), 729–787 (2010).
28. E. Popov and M. Nevieri, "Grating theory: new equations in Fourier space leading to fast converging results for TM polarization," *Journal of the Optical Society of America A-optics Image Science and Vision* **17**(10), 1773–1784 (2000).
29. P. Sheng, R. S. Stepleman, and P. N. Sanda, "Exact Eigenfunctions For Square-Wave Gratings - Application To Diffraction And Surface-Plasmon Calculations," *Phys. Rev. B* **26**(6), 2907–2916 (1982).
30. J. A. Porto, F. J. Garcia-Vidal, and J. B. Pendry, "Transmission resonances on metallic gratings with very narrow slits," *Phys. Rev. Lett.* **83**(14), 2845–2848 (1999).
31. E. Palik and G. Ghosh, eds., *The Electronic Handbook of Optical Constants of Solids* (Academic, New York, 1999).
32. S.-H. Chang, S. Gray, and G. Schatz, "Surface plasmon generation and light transmission by isolated nanoholes and arrays of nanoholes in thin metal films," *Opt. Express* **13**, 3150–3165 (2005).
33. J. A. Dionne, L. A. Sweatlock, H. A. Atwater, and A. Polman, "Plasmon slot waveguides: Towards chip-scale propagation with subwavelength-scale localization," *Phys. Rev. B* **73**(3), 035407 (2006).
34. M. Born and E. Wolf, *Principles of Optics, sixth edition*, sixth edition ed. (Pergamon Press, 1993).
35. J. Weiner and F. D. Nunes, "High-frequency response of subwavelength-structured metals in the petahertz domain," *Opt. Express* **16**(26), 21256–21270 (2008).
36. H. Raether, *Surface Plasmons* (Springer-Verlag, Berlin, 1988).
37. G. L ev eque, O. J. F. Martin, and J. Weiner, "Transient behavior of surface plasmon polaritons scattered at a subwavelength groove," *Phys. Rev. B* **76**(15), 155418 (2007).

1. Introduction

Determining light transmission through small single apertures and periodic aperture arrays might appear to be a straight-forward problem of physical optics. For over a half century, however, a wide range of measurement techniques, theoretical predictions and numerical calculations have resulted in disparate, sometimes contradictory conclusions. The story up to about the beginning of 2009 has been recently reviewed for 1-D slit arrays [?]. This review contains ex-

tensive references to earlier work on light transmission through subwavelength apertures prior to 2009. Published studies of light transmission through subwavelength apertures have continued unabated in 2009 [?, ?, ?, ?, ?, ?, ?] and 2010 [?, ?, ?, ?, ?, ?, ?, ?, ?, ?, ?] with increasing interest in annular or coaxial apertures [?, ?, ?]. Since transmission through apertures is closely related to transmission through wave guides, proper understanding of the relevant physics is critical to new applications such as subwavelength resonant wave guide networks [?]. Another review on transmission through subwavelength apertures and aperture arrays, reflecting the point of view of those authors, has recently appeared [?].

Theoretical approaches to transmission through slit and hole arrays have been developed on the basis of optical grating theory [?], analytic solutions to the scalar Helmholtz wave equation, or Maxwell’s vector field equations on which periodic boundary conditions have been imposed. Numerical approaches such as the transfer matrix method [?, ?] have also been proposed. The results obtained using these methods are often interpreted in terms of modes or bands that are collective properties of the entire array.

Here transmission is examined from the perspective of classical electrodynamics. The scattered electromagnetic (EM) field is calculated numerically using a full three-dimensional (3D) finite-difference-time-domain (FDTD) technique applied to Maxwell’s equations. In addition to the EM fields, the charge current densities induced near the dielectric metal interfaces on the incident surface and within the aperture walls are also determined. These currents are sources for the local magnetic fields (H-fields) that figure importantly in the essential physics of the light transmission through subwavelength structures. We consider a single subwavelength slit and a pair of slits in a Ag film. These two very simple structures bring out most of the relevant physics applicable to periodic arrays with a greater number of elements. Figure ?? shows the geometrical layout and coordinate orientation for the two cases.

2. Transmission through a single subwavelength slit

2.1. General Properties

We calculate the interaction between an electromagnetic plane wave with electric and magnetic field amplitudes E_0, H_0 , centered around a free-space wavelength $\lambda_0 = 514.5$ nm, and a Ag film deposited on a glass substrate with index $n = 1.46$. The index of refraction is symmetric on the entrance and exit interfaces of the Ag film, and the material index of the slit is set to $n = 1.46$ as well. This setup corresponds to an experimental situation in which the Ag film is sandwiched between two glass plates and the apertures are filled with index-matching fluid. The complex permittivity of Ag is taken from a standard compilation [?], and the thickness of the Ag film is set to 200 nm, the same film thickness as in the two-slit transmission studies described in Section ?? . The physical and material parameters chosen for these finite-difference-time-domain (FDTD) simulations are typical of those used in previously reported measurements [?]. The simulations consist in applying the FDTD numerical algorithm to solve Maxwell’s equations in 3D. The results of the calculations are obtained in the form of phasor fields $Fe^{i\phi}$. The results presented here employed a total-field-scattered-field (TFSF) source, although a plane-wave source at various distances from the incident facet was also investigated to insure that the results were not dependent on source position. Perfectly matched layers (PMLs) were used to suppress spurious numerical reflections, and the metal film extended through the PMLs along the X, Y directions to insure this suppression to negligible levels. The overall computational space varied somewhat over the course of these studies, but typical values were $4.5 \mu\text{m}$ in the X direction, $3.5 \mu\text{m}$ in the Y direction, and $3 \mu\text{m}$ in the Z direction. The numerical field solutions were converged to better than one part in 10^5 . The grid size along the X, Y directions was 2 nm and along Z , 5 nm. The dependence of the results on grid size was tested by decreasing the grid increment along X from 2 nm to 1 nm with no change in the calculated

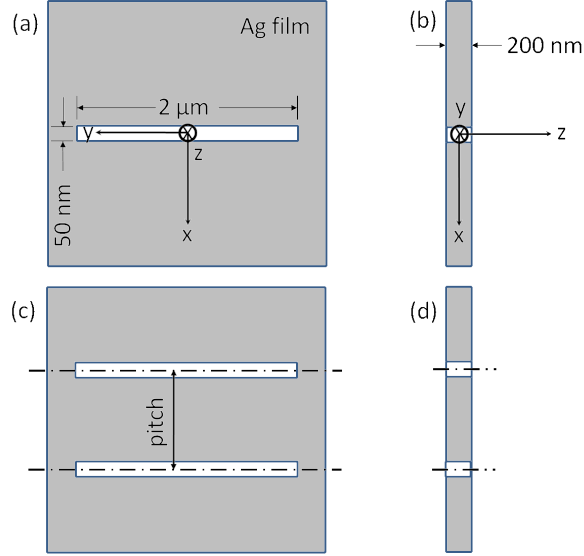


Fig. 1. Schematic of the one- and two-slit structures: (a) Incident surface XY plane with 50 nm slit milled in a 200 nm thick Ag film. (b) Section cut in the XZ plane. (c) Incident surface XY plane of two-slit structure separated by a variable pitch ranging over 3 to 4 wavelengths of the characteristic surface wave generated by light incident normal to the XY plane. (d) Section cut in the XZ plane of the two-slit structure. The dielectric index of refraction surrounding the structures and within the slits is taken to be that of the glass microscope slides used in experiments [?], $n = 1.46$. The plane-wave illumination is taken to be single-frequency at the Ar-ion laser green line, 514.5 nm.

fields to 4 significant figures. Figure ??(a) shows a section cut in the XZ plane of the standing wave set up by an incident plane wave reflected from an unstructured Ag film. The standing wave is established in front of the entrance facet with the maximal H-field amplitude ($\lesssim 2H_0$) adjacent to the interface. The amplitude H_0 is the maximum amplitude of the incident H-field component. The E-field amplitude $\simeq 0$ at the interface, and both E- and H-fields diminish exponentially into the metal. The penetration is characterized by the skin depth, and in the visible region the skin depth of Ag is 25 nm to 30 nm. The slight modulation in amplitude along the X direction is due to the finite spot size of the incident light [?]. Figure ??(b) shows how the field is modified by a 50 nm slit milled into the Ag film. The amplitude of the standing wave around the slit entrance is markedly attenuated, while some light-wave transmission to the exit facet is clearly evident. The third panel, Fig. ?? (c) shows the amplitude of the net scattered field H_{scat} after the reference standing wave, panel (a), has been subtracted from the total scattered field shown in panel (b). The reference, total, and net scattered fields are related by

$$H_{\text{tot}} = H_{\text{ref}} + H_{\text{scat}} \quad (1)$$

The field H_{scat} is obtained by point-for-point matrix subtraction of the reference field H_{ref} from the total field H_{tot} .

The surface waves are clearly evident on the incident and exit facets. Guided waves, propagating within the slit from the entrance to the exit side, are also observed.

Media 1 is a frame from a movie showing how the surface waves emanate from the slit when illuminated by the incident standing wave. The left panel shows the standing wave for reference and the right panel the net scattered H-field. It can be seen quite clearly from the movie that H-

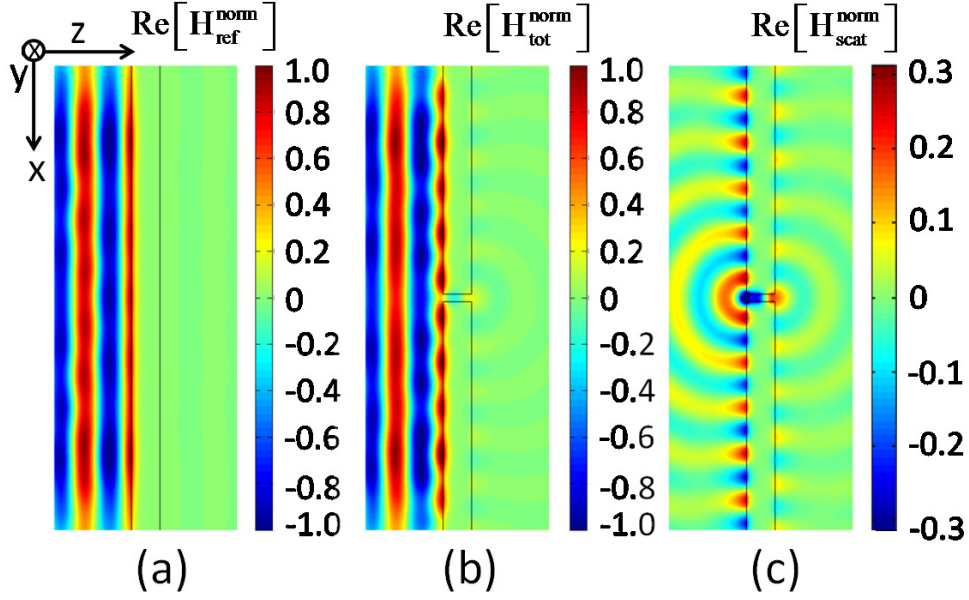


Fig. 2. (a) Reference field amplitude $\text{Re}[H_{\text{ref}}^{\text{norm}}]$, normalized to maximum amplitude $\text{Re}[H_{\text{ref}}^{\text{max}}]$. (b) Total field amplitude $\text{Re}[H_{\text{tot}}^{\text{norm}}]$ normalized as in (a). (c) Net scattered field amplitude $\text{Re}[H_{\text{scat}}^{\text{norm}}]$ normalized as in (a). Note opposite amplitude color code (deep red vs deep blue) between $H_{\text{ref}}^{\text{norm}}$ adjacent to the front Ag facet in panel (a) and $H_{\text{scat}}^{\text{norm}}$ at the slit entrance in panel (c), consistent with phase map in Fig. ?? . Length spans on each panel: $X = 3.2 \mu\text{m}$, $Z = 1.335 \mu\text{m}$.

field components of the surface wave and the standing wave at the unstructured surface appear to be $-\pi$ out of phase. Note also the presence of H-field throughout the slit and the transmission of the EM field from the incident to the exit side. On the the exit surface a second, weaker train of surface waves is evident together with waves propagating into space.

The appearance in Fig. 3 (right panel) of the out-of-phase relation between the scattered wave at the slit entrance and the incident standing wave (left panel) is confirmed by the static phase map of Fig. ?? . This figure shows the phase of H_{scat} in detail around the slit region, relative to that of H_{ref} . The standing wave reference phase has been set equal to zero at the incident surface. The phase values range from $-\pi$ to $+\pi$ radians, and the greatest relative scattered H-field phase, $\varphi_{\text{scat}} = -3.1405$ radians, is located on the slit centerline, about 10 nm to the left of the front facet.

2.2. Effect of Metal Film Thickness on Light Transmission through a Single Slit

Although Media 1 shows significant light transmission through the slit, in fact the transmission depends sensitively on the metal film thickness. The term “transmission” T has a precise meaning. It is the ratio of the Z component of the energy flux (Poynting vector) detected leaving the exit plane, integrated over the area of the detector A_{det} , to the Z component of the energy flux from the source, integrated over the area of the source A_s entering on the incident side.

$$T = \frac{\int_{A_{\text{det}}} P_z dA_{\text{det}}}{\int_{A_s} P_z dA_s} \quad (2)$$

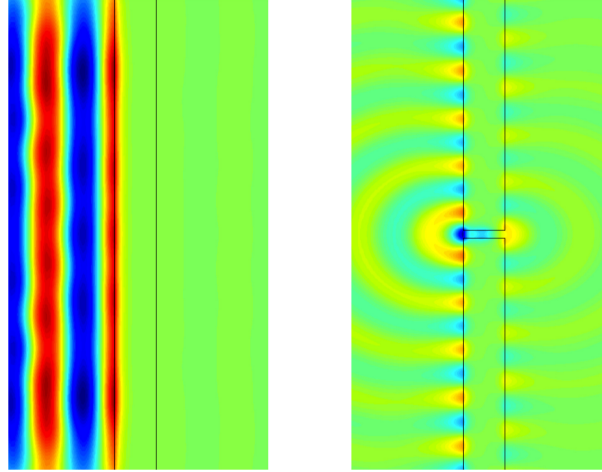


Fig. 3. Frame from Media 1. Left panel shows amplitude $\text{Re}[H_{\text{ref}}^{\text{norm}}]$ and the right panel amplitude of H-field, $\text{Re}[H_{\text{scat}}^{\text{norm}}]$. The surface waves propagate along the two dielectric-metal interfaces. After about two optical cycles they appear to stabilize in amplitude and phase. Length span $X = 3.2 \mu\text{m}$, $Z = 1.335 \mu\text{m}$.

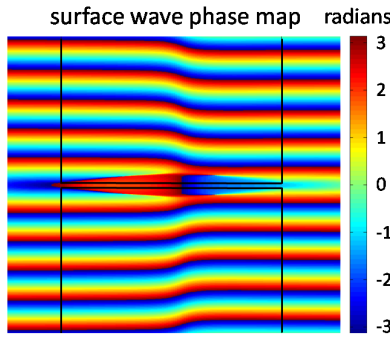


Fig. 4. Phase map of H_{scat} relative to H_{ref} . The color bar limits are $\pm\pi$ radians. Along the slit centerline the point of maximum phase is 10 nm to the left of the vertical surface line. At that point $\varphi_{\text{scat}} = -3.1405$ radians. The map also shows the phase variation of the waves propagating on the incident and exit surfaces and the spatial variation of the phase within the slit volume. Spatial dimensions: vertical, $X = 3.2 \mu\text{m}$; horizontal, $Z = 0.300 \mu\text{m}$.

where P_z is the component of the Poynting vector perpendicular to the metal planes. One is usually more interested in the ratio of P_z exiting the slit to P_z illuminating the slit on the input side rather than the energy flux from the source. The “normalized” transmission T_{norm} is the ratio of the energy flux detected on the exit side to the energy flux passing through the cross sectional area of the slit.

$$T_{\text{norm}} = \frac{\int P_z dA_{\text{det}}/A_{\text{slit}}}{\int P_z dA_s/A_s} = T \frac{A_s}{A_{\text{slit}}} \quad (3)$$

The size and position of A_{det} was varied to insure the invariance of T . Figure ?? shows the calculated transmission through a $2 \mu\text{m}$ long slit, 50 nm wide (Fig. ??), over a range of thickness from 100 nm to 350 nm. The two maxima correspond to Fabry-Perot-like resonances within the slit volume for the first half-wave and full wave of the light within the slit. Note that the

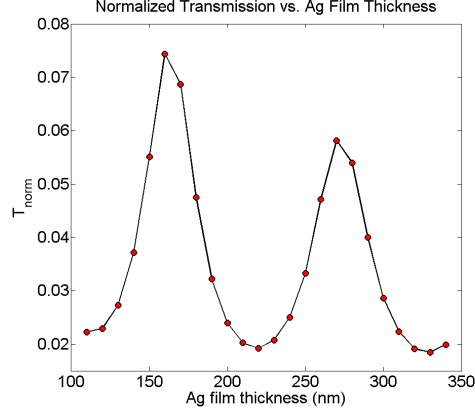


Fig. 5. Calculated transmission T_{norm} through a single subwavelength slit as a function of metal film thickness. The peaks are due to Fabry-Perot cavity resonances set up within the slit volume.

transmission ratio from the peak around 161 nm thickness to baseline is $\simeq 3.5$.

Figure ?? shows plots of the total E- and H-field intensities along the Z axis within the slit and along the slit centerline for the two maxima. The first transmission maximum corresponds to a standing half-wave E-, H-field with E-field maximum intensity at the slit center; while the second transmission maximum corresponds to a standing full wave with an E-field intensity node at the center. From the positions of the E-field peaks and the H-field nodes in Fig. ?? we can calculate the effective wavelength of the standing wave and therefore the effective wavelength of the propagating mode in the cavity. We find $\lambda_{\text{eff}} = 228$ nm, and the effective index of refraction within the slit $n_{\text{eff}} = 1.54$. This effective index is 5.5% higher than $n = 1.46$. The transverse profile of the propagating mode in the slit is the lowest order symmetric “plasmon slot wave guide mode” discussed by Dionne et al. [?].

From the ratio of the transmission at the slit exit and entrance, τ , we can apply a Fabry-Perot analysis to obtain the absorptive loss \mathcal{A} within the cavity, the reflectivity \mathcal{R} and the finesse \mathcal{F} [?].

$$\tau = \left(1 - \frac{\mathcal{A}}{1 - \mathcal{R}}\right)^2 \quad (4)$$

$$\mathcal{F} = \frac{\pi\sqrt{\mathcal{R}}}{1 - \mathcal{R}} \quad (5)$$

We determine from the first transmission maximum the reflectivity $\mathcal{R} = 0.58$ and a finesse $\mathcal{F} = 5.7$. Clearly this Fabry-Perot “etalon” exhibits low finesse due to the small index contrast between the interior of the slit and the incident and exit space and absorptive loss in the metal walls as the propagating mode passes through the slit.

2.3. Current densities on the front facet and in the slit walls

The presence of the standing wave on the front facet results in the harmonically time-varying H-field adjacent to the metal, inducing charge currents at and just below the surface. When discontinuities in the surface are present, such as slits or holes, these currents “charge” the edges just as an oscillating current charges a capacitor. The result is an oscillating charge density

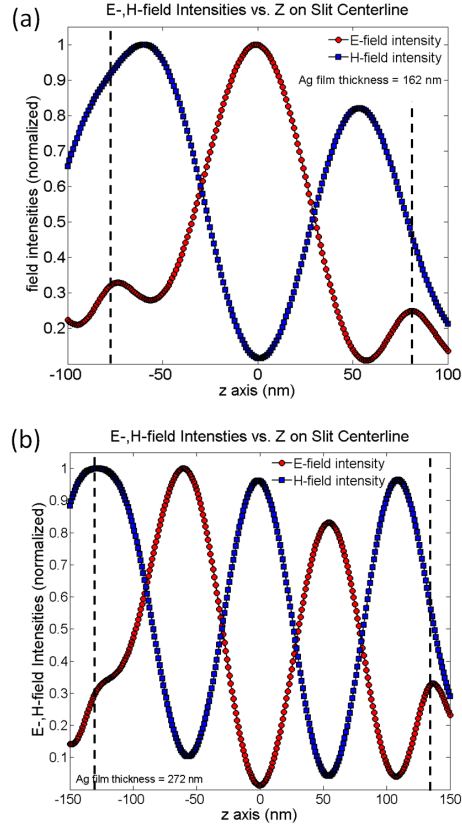


Fig. 6. (a) Filled red circles: calculated E-field intensity; filled blue squares: calculated H-field intensity along Z on the slit centerline (see Fig ?? b) for Ag film thickness of 162 nm. Dashed vertical lines indicate the position of the incident and exit Ag film XY planes. (b) Same plot as (a) but for Ag film thickness of 272 nm. The out-of-phase intensity distribution between E- and H-fields indicates a standing wave within the slit.

dipole near the slit corners on the incident side. The presence of this charge dipole also induces current flow along the slit walls, and these oscillating wall currents function as local sources for the H-fields within the slit. Media 2 illustrates the influence of the induced currents J_x, J_z , acting as a local sources for the EM fields present near and within the slit volume.

The current density components J_x, J_z are calculated from the E-field components using the proportionality of current to field in good conductors,

$$J_x = \sigma E_x \quad \text{and} \quad J_z = \sigma E_z \quad (6)$$

where σ is the conductivity of the metal. These E-field components are nonnegligible within the skin depth near the metal-dielectric interfaces. The conductivity σ_{Ag} of the metal is complex, and at optical frequencies the imaginary part is dominant [?]. The result is that the oscillating current density along the front facet (J_x) is in phase with the reference H-field as can be easily seen in Media 2. The currents J_z running in the slit walls, Fig. 7(c), are the source of the H-field within the slit near the entrance, oscillating in opposite phase to H_{ref} .

The amplitude of H_{scat} within the slit just at the entrance (Fig. ?? d) is about 62 % of the reference field H_{ref} , and the amplitude of the surface waves traveling along $\pm x$, away from the

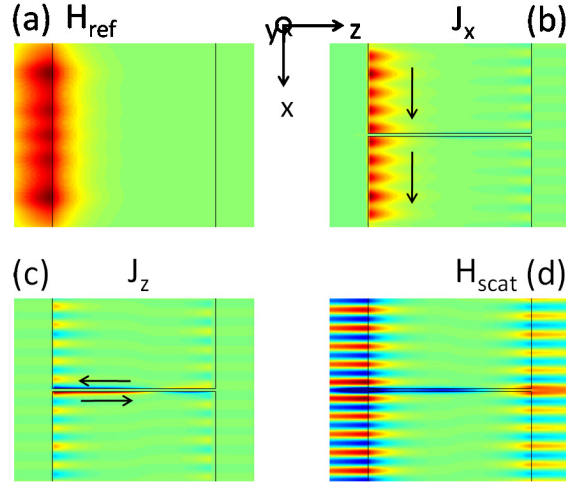


Fig. 7. Media 2 frame showing: (a) standing wave resulting from reflection of an incident plane wave on a plane Ag surface. (b) A component of the induced current density running near the incident surface in the positive X direction. (c) Current density components running in the slit wall along the Z direction. (d) Amplitudes of H_{scat} , normalized to the maximum amplitude of H_{ref} , produced by the current density components. Color code: red, green, blue; positive, null, negative amplitudes, respectively.

slit origin on each side, is about 25% of H_{ref} . Figure ?? plots the amplitude of the surface wave 2 nm in front of the incident facet. The plot shows the relatively strong negative amplitude just above the slit entrance and the amplitudes of the regularly spaced surface waves propagating away from the slit on either side. It is worth noting that the wavelength of the surface waves is not quite regular, $\simeq 318$ nm at the periphery and slightly shorter, about $\simeq 308$ nm, in the immediate vicinity of the slit. The surface plasmon polariton (spp) wavelength, calculated from the Raether formula [?] and from the tabulated material constants of Ag [?] is $\lambda_{\text{spp}} = 309.4$ nm.

3. Transmission in two-slit arrays

Adding a second slit to the structure sets up an interaction between the two slits that modulates the transmission intensity as a function of slit separation. Figure ??(c) shows the basic layout for the numerical simulations and Fig. ?? shows the log (base 10) of the calculated transmission as a function of slit separation. The plot is normalized to the transmission from a single slit.

The modulation clearly shows minima at slit separations very close to integral numbers of surface wave wavelengths (calculated from the Raether formula [?]) for spp waves $\simeq 309$ nm. The two-slit phase map of H_{scat} in Fig. ?? shows that the magnetic field component of the surface waves is $-\pi$ out of phase with respect to the incident standing wave, H_{ref} , and therefore partially cancels H_{ref} when the slits are separated by an integer number of surface-wave wavelengths. Thus interference between the surface wave and the standing wave established at the incident metal-dielectric boundary is the primary effect controlling the transmission modulation traced out in Fig. ??.

This interference is explicitly illustrated in Fig. ?. The figure plots the absolute value of the H-field components of the total field H_{tot} , the incident field H_{ref} and the net scattered field H_{scat} related by Eq. (?). Panel (a) shows the amplitude of the H-field component of the inci-

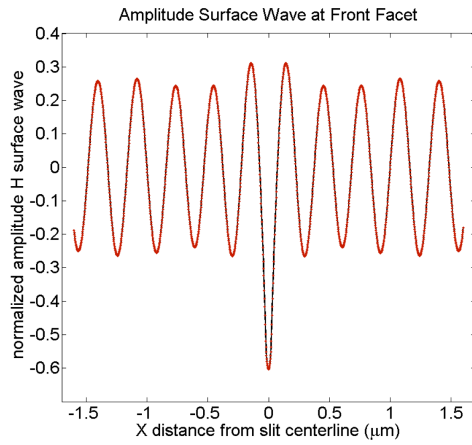


Fig. 8. Amplitude of H_{scat} , normalized to H_{ref} at the surface plotted against the distance on either side of the slit centerline. The plot corresponds to a vertical cut in Fig. 7(d), 2 nm to the left of the front facet.

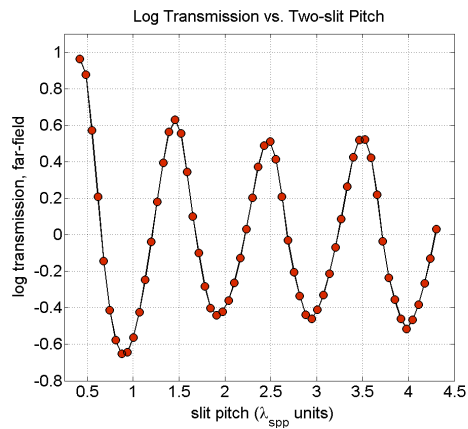


Fig. 9. Log (base 10) of transmission as a function of slit separation for a two-slit array. The transmission is normalized to that of a single slit. Slit dimensions are the same as in the one-slit studies. The intensity modulation pattern shows minima very close to integral numbers of the Raether $\lambda_{\text{spp}} = 309.4$ nm.

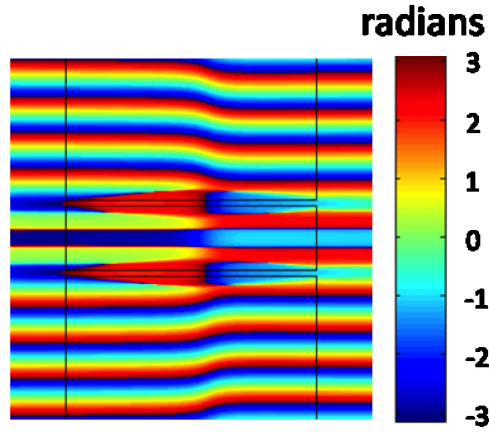


Fig. 10. Phase map of the scattered H-field (H_{scat}) relative to the phase of the standing wave H-field (H_{ref}) for a two-slit structure separated by 618 nm, twice the spp wavelength of $\lambda_{\text{surf}} = 309$ nm. The color bar limits are $\pm\pi$ radians. The map shows that the surface wave phase is very close to $-\pi$ radians at the position of the slits, that a standing wave sets up between the slits, and that surface waves propagate away from the slits on the sides exterior to the slit pair. Spatial dimensions same as in Fig. ??

dent standing wave H_{ref} close to the dielectric-metal interference on an unstructured surface. Panels (b), (d) show H_{tot} in the vicinity of two-slit structures. Panel (b) specifies a centerline-to-centerline slit separation of 618 nm ($2\lambda_{\text{spp}}$), a position of transmission minimum in Fig. ??, while panel (d) shows the same field component at a slit separation of 772.5 nm ($2.5\lambda_{\text{spp}}$), near a position of transmission maximum. Panels (c), (e) show the net scattered field around the same slit layouts. When the two slits are separated by an integral number of surface wave wavelengths, the surface waves issuing from each slit arrive at the site of its neighbor nearly an integral number of π radians out of phase with the reference standing wave. The resulting destructive interference minimizes the local H-field and the consequent local currents and charge dipoles that are responsible for transmission to the exit side. A standing surface wave is established between the slits, and the surface waves propagate away from the slits on the sides exterior to the slit pair in the $\mp X$ directions. Note in panel (b) of Fig. ?? the strong cancellation of the total field on the incident side at the position of the slits and the consequent weak scattered field within the slits and on the exit side in panel (c). Note also that panel (c) shows significantly more scattered surface-wave field, compared to panel (e), along the incident interface. The reason is that slit separations minimizing transmission must maximize reflection, and reflection can appear either as propagating or surface waves traveling back along $-Z$ and $\pm X$. In contrast to panels (b), (c) the field components shown in panels (d), (e) exhibit strong total and scattered fields within the slits and on the incident and exit surfaces. Note the strong standing surface waves between the slits on both sides of the Ag film. The transmission through the slits of the scattered waves at conditions of minimal and maximal transmission can be visualized through the animation of [Media 3](#).

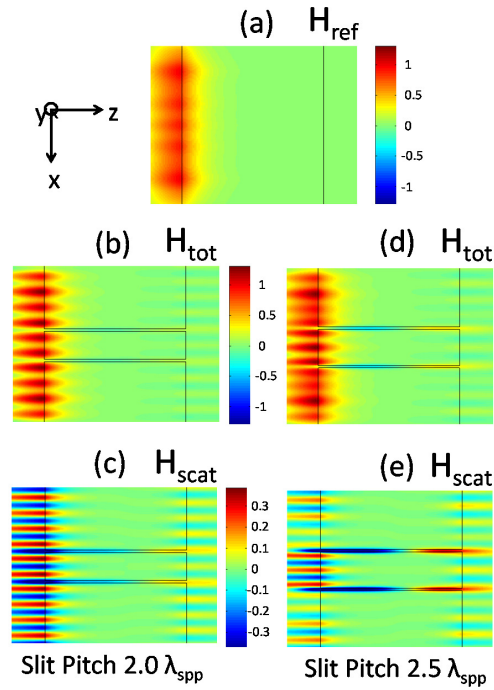


Fig. 11. Panel (a): H-field amplitude of the reference standing wave, H_{ref} , on the plane Ag surface. Color bar spans maximum and minimum field amplitude. The two vertical black lines denote the Ag film thickness, 200 nm. Note that H_{ref} has maximum amplitude adjacent to the surface and penetrates the metal to the skin depth. Panels (b), (c): Amplitude of the total H-field (H_{tot}) and scattered H-field H_{scat} , respectively, with slit pitch equal to $2\lambda_{\text{spp}}$. Note relatively strong scattered field on incident surface, weak field within slits, and minimal transmission at this slit pitch. Panels (d), (e): H_{tot} , H_{scat} with slit pitch $2.5\lambda_{\text{spp}}$ near transmission maximum. Length span $X = 3.2 \mu\text{m}$, $Z = 0.300 \mu\text{m}$.

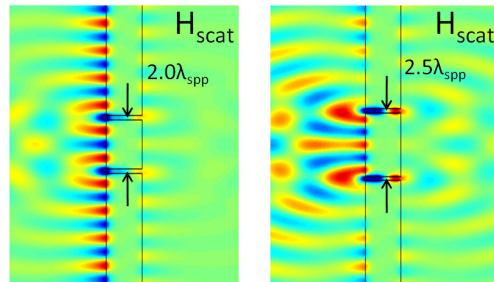


Fig. 12. Frame from Media 3. Left panel: H_{scat} on two-slit structure with slit pitch of $2\lambda_{\text{spp}}$. Note strong amplitude of scattered surface waves on the incident facet propagating away from the slits in $\pm X$ direction and relatively weak transmitted propagation to the exit side. Right panel: H_{scat} on two-slit structure with slit pitch of $2.5\lambda_{\text{spp}}$. Note large standing wave on entrance facet between slits, strong field in the slit and relatively strong amplitude of transmitted propagating wave. Color code: red, green, blue; positive, null, negative amplitudes, respectively.

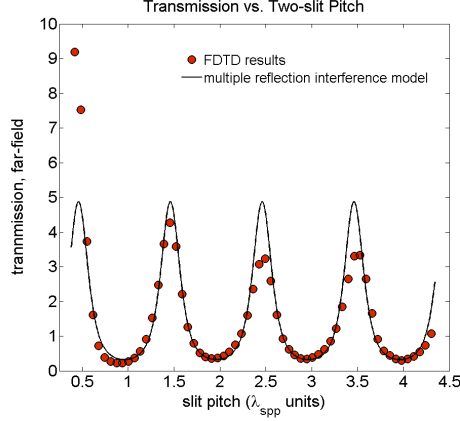


Fig. 13. Plot of FDTD results for far-field transmission through two slits (solid circles) and a fit of Eq. (7) to the FDTD calculation (solid line).

4. Comparison of FDTD results to interference models and measurements

4.1. Comparison to models

A simple model for the transmission profile has been proposed [?] that takes into account interference between the incident and surface waves on the entrance facet, transmission through the slits, and interference on the exit facet between the guided waves emerging from each slit and the surface waves produced by them on the exit side of the Ag film. The expression for the transmission in the far-field, taking into account multiple reflections at slit openings on the front and back surface, Eq. (5) of Ref. [?], is

$$\eta^{(\infty)}(p) = \left\{ 1 + (\beta_0 \beta'_0)^2 - 2\beta_0 \beta'_0 \cos \left[\left(\frac{2\pi}{\lambda_{\text{spp}}} \right) p + \varphi \right] \right\}^{-2} \quad (7)$$

where β_0 is the fraction of the incident amplitude converted to surface waves at a given slit and β'_0 is the fraction of the surface wave amplitude reconverted to a propagating mode at the opposite slit, p is the pitch, λ_{spp} is the surface plasmon polariton wavelength, and φ is the phase of the surface wave with respect to the incident H-field. The product of the two coefficients β_0, β'_0 is treated as a single parameter and essentially functions as the “reflectivity” in a Fabry-Perot resonator. Figure ?? shows a nonlinear least-squares fit of Eq. (7) to the FDTD results. The values of $\beta_0 \beta'_0$ and φ used to obtain the best nonlinear least squares fit are $\beta \beta' = 0.49$ and $\varphi = -0.91\pi$, respectively. The best-fit phase parameter is reasonably consistent with the FDTD results of $\varphi = -0.97\pi$.

The interference expression of Eq. (7) does not take into account the short-lived, transient surface waves that are present close to the slit origin [?] or the absorptive losses due to the Ag metal. In order to account for these effects we have modified the transmission expression of Eq. (7),

$$\eta_{\text{mod}}^{\infty}(p) = \left\{ \left(1 + k_0 e^{-k_1 p} \right)^2 e^{-2k_{\text{Ag}} p} (\beta \beta')^2 - 2 \left(1 + k_0 e^{-k_1 p} \right) \left(e^{-k_{\text{Ag}} p} \right) \beta \beta' \cos (2\pi k_2 p + \varphi) \right\}^{-2} \quad (8)$$

The term $1 + k_0 e^{-k_1 p}$ represents the rapid decay of unstable surface wave transients close to the slit center and the factor $e^{-k_{\text{Ag}} p}$ represents slow decay due to absorptive dissipation of the

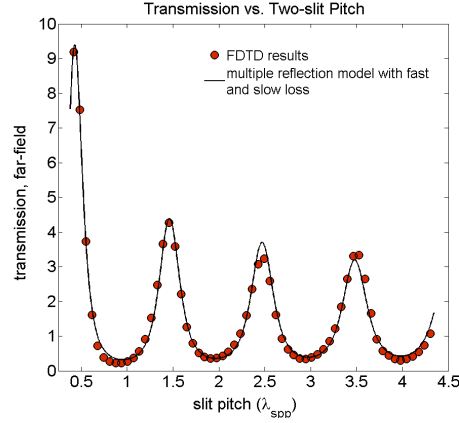


Fig. 14. Lossy multiple reflection model fit, Eq. (??), to FDTD results (solid circles).

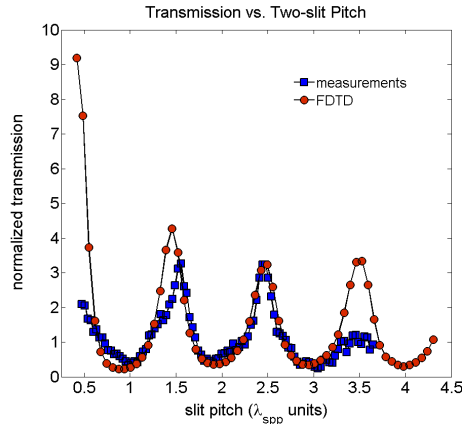


Fig. 15. Comparison of measured transmission [?] to FDTD numerical simulations.

stable surface wave as it propagates along the Ag surface. The value of $k_{Ag} = 0.0805 \lambda_{spp}^{-1}$ units, is calculated from the Raether formula [?] using the imaginary part of the Ag permittivity [?]. The factor k_2 was inserted to allow for best-fit scaling of the surface wave wavelength and φ is again the phase of the surface wave relative to the reference field.

Figure ?? show the results of the nonlinear least squares fitting. The best-fit values for $\beta_0 \beta'_0$ and φ are $\beta_0 \beta'_0 = 0.33 \pm 0.01$ and $\varphi = -0.88\pi \pm 0.01$. The other parameters are found to be $k_0 = 0.8 \pm 0.3$, $k_1 = 2.0 \pm 0.9 \lambda_{spp}$ units, $k_2 = 0.987 \pm 0.003 \lambda_{spp}$ units. The \pm values are 95 % confidence limits. With this modified model φ is still close to $-\pi$, and the value of k_1 implies that the transient surface modes damp away $\sim \lambda_{spp}$. From the best-fit scaling of the surface wave wavelength we find $\lambda_{surface} = 313$ nm, slightly longer than λ_{spp} (309 nm). The good overall fit of Eq. (??) to the FDTD “data” inspires confidence that the “lossy multiple reflection interference” model captures the essential physics of optical transmission through subwavelength slits.

4.2. Comparison to measurements

Quantitative measurement of optical transmission profiles for slit arrays as a function of slit separation and array elements have already been reported [?]. Figure ?? shows the measured

transmission intensity for an array of two slits and the present 3-D FDTD simulation results with very similar optical, geometrical, and material parameters. The general features of maxima and minima positions are in agreement, but the measurements show more marked amplitude fluctuations than the FDTD results. This is hardly surprising since real experiments involve measurement uncertainties to which numerical computations are not subject. In particular the experiments collected transmitted light in the far field through a microscope objective, and the efficiency of this collection may vary with slit separation. This variation might possibly be the reason for disparity between the measured and simulated transmission amplitudes around the peak at $3.5\lambda_{\text{spp}}$ units. Improved experimental control of critical measurement parameters would permit comparison not only of maxima and minima positions but also the amplitude and line shape of the transmission profile. Confirmation of the Fabry-Perot-like transmission profile would lend further credence to the lossy multiple reflection model.

5. Summary

We have reported here a numerical study of the light transmission through a single slit and the transmission profile as a function of slit separation for light issuing from two subwavelength slits milled in a Ag metal film. The parameters of illumination wavelength, slit width, dielectric and metal material properties were all chosen to allow simulations to match as closely as possible experiments performed earlier [?]. The numerical solution to Maxwell's equations was carried out using a 3-D, FDTD numerical algorithm. The simulations reveal how the transmission profile is controlled principally by interference between the standing wave and surface waves at the front facet as well as interference at the exit side between light emerging from the slits and surface waves propagating on the back surface. In addition a weak Fabry-Perot multiple reflection effect within the slits leads to significant modulation of the transmission as a function of metal film thickness. When the slit separation is near half-integer multiples of λ_{spp} , and the film thickness is near half- or full-integer wavelengths of the guided mode within the slit "cavity," optimal transmission is achieved. Surface waves are launched at the slit sites on the incident facet with fairly high efficiency ($\sim 55\%$ of the incident amplitude) and the physical basis of the "launch" is local charge density dipoles accumulating at the slit corners from induced currents within the skin depth of the front metal surface. These currents are induced by the harmonically oscillating standing-wave H-field that is established at the dielectric-metal interface. The charge dipoles built up at the corners on the front face also induce charge currents running in the slit walls that serve as local sources of H-field within the slits. *The direction of these induced charge currents, J_x, J_z synchronously converging toward and diverging away from the slit corners, produce H-fields at openings and within the slits $-\pi$ out of phase with respect to the reference H-field.* Fitting a lossy, multiple reflection interference model to the FDTD results reproduces all the features of the numerically calculated transmission profile. The fitting parameters $\beta\beta'$ and ϕ , the surface-wave conversion efficiency and surface-wave phase, are consistent with the directly calculated FDTD data. Finally comparison with previously published results for slit transmission show good agreement with the position of nodes and antinodes but significant differences in the interference fringe contrast and detailed shape of the line profile. Further work on reducing experimental uncertainties, improving and refining the earlier results appears warranted.

Acknowledgments

D. Pacifici and H. Lezec are thanked for invaluable discussions. A two-year visiting fellowship from the University of Maryland Institute for Research in Electronics and Applied Physics (IREAP) and the Center for Nanoscale Science and Technology (CNST) of the National Institute of Standards and Technology (NIST) is gratefully acknowledged.